Nano Research
https://doi.org/10.1007/s12274-017-1773-2
Research Article
ISSN 1998-0124
CN 11-5974/O4

Device performance and light characteristics stability of quantum-dot-based white-light-emitting diodes

Bruno Clasen Hames, Iván Mora-Seró, and Rafael S. Sánchez[†] (✉)

Institute of Advanced Materials (INAM), Universitat Jaume I, 12071 Castelló, Spain
[†] *Present address: Department of Chemistry, University of Liverpool, Crown St., L69 3BX, Liverpool, United Kingdom*

Received: 10 March 2017
Revised: 21 July 2017
Accepted: 21 July 2017

KEYWORDS
colloidal quantum dots, quantum dot light-emitting diodes, white light-emitting diode (LED) displays, electroluminescence, LED stability

ABSTRACT

Advances in image quality in recent decades have made it necessary to develop new technologies for producing displays to meet remarkably stricter standards. The display market is governed mainly by liquid crystal display and light-emitting diode (LED) technology; however, it suffers from limitations that can be overcome by developing the next generation of electroluminescent displays. The introduction of colloidal quantum dots (QDs) as down-converters has enabled the production of displays with extremely high color purity and gamut. Therefore, colloidal nanocrystals are excellent candidates for the preparation of electroluminescent devices, which represent a straightforward approach to the development of unprecedented high-quality displays. We synthesized light-emitting QDs covering the entire visible spectrum with high fluorescence quantum yields and color purity, and produced high-brightness single-color LEDs with external quantum efficiencies of 0.39%, 1.04%, 2.10%, and 1.30% for red-, orange-, green-, and blue-emitting dots, respectively. Additionally, white LEDs were prepared by mixing QDs; they showed color temperatures of 5,300 K and color rendering indices exceeding 80%. Very importantly, we exhaustively characterized the LED performance, including the response time, stability, and evolution of the light characteristics, thus providing crucial information toward the development of high-quality electroluminescent displays.

1 Introduction

Colloidal quantum dots (QDs) have attracted great attention in the scientific community since they were first reported [1] owing to their unique properties, which make them suitable for a wide range of applications, e.g., medical applications [2, 3] or optoelectronics [4, 5]. Because of their excellent semiconductor properties, colloidal QDs have been employed recently for the preparation of highly efficient photovoltaic devices [6–9], photodetectors [10–13], and light-emitting diodes (LEDs) [14–19]. In particular, visible-light-emitting QDs with core–shell structure are excellent candidates for the development of light-emitting devices because they

Address correspondence to rasanche@uji.es

show extremely high fluorescence quantum yields ($\Phi_f \approx 1$), color tunability depending on the particle size and composition, extremely narrow emission spectra, and high thermal and photostability [20, 21]. In fact, QDs have recently entered the market for the preparation of high-color-purity and wide-gamut displays [22]; however, these displays exploit liquid crystal display (LCD) and LED technology, using blue-emitting diodes as back-illumination and QDs, typically green and red, as down-converters to produce a wide palette of colors. On the one hand, LCD-LED technology provides devices with very intense luminosity. On the other hand, the introduction of QDs allows the production of displays with high color purity and a wide color gamut; however, the back-illumination required in this approach limits the purity of the color black, which implies that the image contrast is relatively limited. In addition, the use of a back-illumination system increases the total thickness of the display. The breakthrough required for the development of the next generation of high-quality displays is expected to consist of a matrix of individually controllable multicolored pixels, as in organic LED (OLED) technology, but in this case using inorganic colloidal QDs as light-emitting materials. To date, QDs have yielded electroluminescent devices with excellent external quantum efficiencies (EQEs), and, very importantly, the color gamut of the displays can be extended greatly owing to the outstanding color purity of the emitted light [23]. In addition, the image contrast of OLED or QD-LED electroluminescent devices is far larger than that of any other existing technology based on the back-illumination approach, as the color black arises from inactive pixels.

In recent years, significant advances have been achieved not only in the synthesis of excellent quality QDs with emission covering the entire visible spectrum, but also in the fabrication of highly efficient light-emitting devices. In 2013, Mashford et al. reported the fabrication of red-emitting LEDs with current efficiencies of 19 $Cd \cdot A^{-1}$ and an impressive EQE of 18% by exploiting an inverse device configuration and using core–shell CdSe/CdS QDs as the emitting layer [14]. The same year, Lee et al. described the preparation of blue-emitting devices based on CdZnS/ZnS QDs in a standard configuration using poly(3, 4-ethylenedioxythiophene)-polystyrenesulfonic acid (PEDOT:PSS) as a hole-injecting layer (HIL), poly(9-vinylcarbazole) (PVK) as a hole transport material (HTM), and ZnO nanoparticles as an electron transport material (ETM), which showed a maximum luminance of 2,624 $Cd \cdot m^{-2}$, a current efficiency of 2.2 $Cd \cdot A^{-1}$, and an EQE of 7.1% [15]. One year later, Lee et al. continued their work focused on the preparation of green-emitting multishell CdSe/ZnS/ZnS QDs and the subsequent fabrication of devices with a current efficiency of 46.4 $Cd \cdot A^{-1}$ and an EQE of 12.6% [16]. In 2015, Yang et al. described the preparation of red-, green-, and blue-light-emitting devices with maximum currents and EQEs of 15 $Cd \cdot A^{-1}$ and 12.0% for red, 63 $Cd \cdot A^{-1}$ and 14.5% for green, and 4.4 $Cd \cdot A^{-1}$ and 10.7% for blue devices, respectively [24]. In 2015, Lee et al. reported the fabrication of white-light-emitting devices (WLEDs) based on red, green, and blue (RGB) mixed QD layers that showed record performance: a luminance of 23,352 $Cd \cdot m^{-2}$, a current efficiency of 21.8 $Cd \cdot A^{-1}$, and an EQE of 10.9% [25]. Although these earlier works focused on the preparation of high-performance LEDs based on QDs, and subsequent studies focused on overcoming their main limitations, real applications and ultimate commercialization require a deeper understanding of several key aspects, including the stability under working conditions [26, 27], the exact origins and mechanisms of electroluminescence (EL) quenching or degradation [28], the response time of on–off operation [29], and the evolution of the light characteristics during long operation periods [23]. In addition, several approaches have been proposed in the literature aimed at obtaining white LEDs with tunable light properties, among them: 1) methods based on combining different QDs, probably the simplest method that allows reliable control of the loading ratios of the QDs with differentiated emission [25, 30]; 2) deposition of alternating patterned layers of different QDs, which requires the development of more sophisticated deposition techniques [31]; 3) embedding the QDs in an insulating polymer matrix to avoid photoluminescence (PL) self-quenching, which in turn reduces the conductivity of the layer and therefore introduces an inherent limitation [32]; 4) using QD composites to exploit their properties as phosphors, which requires the presence of a short-

wavelength back-illumination LED [33].

In this work, we synthesized highly fluorescent core–shell light-emitting QDs (red, orange, green, and blue) with different chemical compositions by modifying standard procedures [15, 34]. Additionally, we fabricated and exhaustively characterized not only the corresponding single-color LEDs, but also WLEDs prepared by mixing RGB or orange, green, and blue (OGB) QDs.

2 Experimental

2.1 Materials

All the materials employed in this work were used as received from the commercial suppliers. The precursors and solvents employed for QD synthesis were purchased from Sigma-Aldrich, as follows: CdO (99.99%), $Zn(OAc)_2$ (99.99%), oleic acid (OA) (90%), S (99.99%), Se (99.99%), 1-octadecene (ODE) (90%), trioctylphosphine (TOP) (90%), hexane (≥ 95%), acetone (≥ 99.9%), and ethanol (absolute). Prepatterned indium tin oxide (ITO) substrates (20 × 20 mm^2) were purchased from Thin Film Devices. PEDOT:PSS (Al4083) was purchased from Heraeus Clevios, and PVK (M_n 25,000–50,000) and Al:ZnO nanoparticles were acquired from Sigma-Aldrich.

2.2 Synthesis of blue-light-emitting QDs

The synthesis of blue-light-emitting QDs is described in Ref. [15]. In the procedure, 1 mmol of CdO (0.1284 g), 10 mmol of $Zn(OAc)_2$ (1.8348 g), and 7 mL of OA were poured into a 50 mL three-necked flask and degassed under vacuum (10^{-4} bar) at 150 ˚C for 20 min. Then, 15 mL of ODE was added to the mixture, which was further heated to 310 ˚C. A stock solution of 1.6 mmol of S (0.0513 g) in 2.4 mL of ODE was swiftly injected into the reaction flask, and the temperature was maintained for 12 min for core growth. Note that the S stock solution was first placed in an ultrasonic bath for 20–30 min to dissolve the powder completely. Next, a second stock solution of 4 mmol of S (0.1283 g) in 5 mL of OA was added dropwise (0.5 mL·min^{-1}), and the reaction proceeded for 3 h at the same temperature for shell growth. When the reaction time was complete, the crude was cooled in an ice bath. Hexane (20 mL) was added, and the mixture was transferred to a centrifuge tube. Then, 100 mL of analytical-grade acetone was added to precipitate the QDs. The suspension was centrifuged at 4,700 rpm. for 10 min, and the supernatant was discarded. The solid was dispersed in 10 mL of hexane, and 40 mL of absolute ethanol was added to precipitate the QDs; the suspension was then centrifuged using the conditions described above. The redispersion–precipitation procedure was repeated two more times. Finally, the solid was dried under vacuum and weighed to prepare a solution with the desired concentration in hexane (5 mg·mL^{-1}).

2.3 Synthesis of green- and orange-light-emitting QDs

This methodology was previously described in Ref. [34], although we introduced several modifications. In a typical synthesis of green-light-emitting QDs, 0.4 mmol of CdO (0.0514 g), 4 mmol of $Zn(OAc)_2$ (0.7339 g), 17.6 mmol of OA (4.9713 g), and 20 mL of ODE were placed in a 100 mL round flask. The mixture was heated to 150 ˚C and degassed under vacuum (10^{-4} bar) for 20 min; the flask was then filled with N_2 gas and further heated to 310 ˚C to form a clear solution of $Cd(OA)_2$ and $Zn(OA)_2$. Separately, a stock solution of 0.1 mmol of Se powder (0.0079 g) and 4 mmol of S powder (0.1283 g) in 3 mL of TOP was prepared under N_2 (after the Se and S were sonicated for 20–30 min to completely dissolve them). The Se/S solution was quickly injected into the reaction flask at 310 ˚C. Next, the temperature of the reaction flask was set to 300 ˚C for 10 min to promote QD growth; the flask was then cooled quickly to room temperature by immersion in an ice-water bath to stop the growth. Hexane (20 mL) was added, and the obtained mixture was transferred to a centrifuge tube. Then, 100 mL of analytical-grade acetone was added to precipitate the QDs. The suspension was centrifuged at 4,700 rpm. for 10 min, and the supernatant was discarded. The solid was dispersed in 10 mL of hexane, and 40 mL of absolute ethanol was added to precipitate the QDs; the suspension was then centrifuged using the conditions described above. The redispersion–precipitation procedure was repeated two more times. Finally, the solid was dried under vacuum and weighed to prepare a solution with the desired concentration in hexane (5 mg·mL^{-1}).

For the synthesis of orange-light-emitting QDs, the ratio of Se/S was modified; a stock solution of 1 mmol of Se (0.0789 g) and 2.3 mmol of S (0.0738 g) in 3 mL of TOP under N_2 was prepared.

2.4 Synthesis of red-light-emitting QDs

First, 0.4 mmol of CdO (0.0514 g), 4 mmol of $Zn(OAc)_2$ (0.7339 g), 17.6 mmol of OA (4.9713 g), and 20 mL of ODE were placed in a 100 mL round flask. The mixture was heated to 150 ˚C and degassed under vacuum (10^{-4} bar) for 20 min; the flask was then filled with N_2 gas and further heated to 300 ˚C to form a clear solution of $Cd(OA)_2$ and $Zn(OA)_2$. Separately, a stock solution of 1 mmol of Se powder (0.0789 g) in 1.5 mL of TOP was prepared under N_2 (after the Se was sonicated for 20–30 min to completely dissolve it). The Se solution was quickly injected into the reaction flask at 300 ˚C and reacted for 30 s before the sulfur precursor was added. Then, a second stock solution of 2.3 mmol of S (0.0738 g) in 1.5 mL of TOP prepared under N_2 was swiftly injected, and the reaction proceeded for 5 min. When the reaction time was complete, the crude was cooled in an ice bath; 20 mL of hexane was added to the mixture, and the resulting solution was transferred to a centrifuge tube. Then, 100 mL of analytical-grade acetone was added to precipitate the QDs. The suspension was centrifuged at 4,700 rpm. for 10 min, and the supernatant was discarded. The solid was dispersed in 10 mL of hexane, and 40 mL of absolute ethanol was added to precipitate the QDs; the suspension was centrifuged using the conditions described above. The redispersion–precipitation procedure was repeated two more times. Finally, the solid was dried under vacuum and weighed for preparing a solution of the desired concentration in hexane (5 mg·mL^{-1}).

2.5 Preparation of the QD-based LEDs

The ITO substrates were placed in a soap solution and sonicated for 5 min. Then the substrates were rinsed, first with Milli-Q water and second with ethanol. Next, they were introduced into a solvent mixture consisting of isopropanol:acetone (1:1 *v*/*v*) and sonicated for 5 min. They were then rinsed with ethanol and dried with compressed air. Then, the substrates were introduced into a UV-O_3 cleaner for 30 min, and a PEDOT:PSS solution was spun-cast at 3,000 rpm. for 60 s and treated at 150 ˚C for 30 min in air, to yield a thin layer (20 nm). Next, a PVK layer (20 nm) was deposited by spin-casting a solution of 10 mg·mL^{-1} of PVK in chlorobenzene at 3,000 rpm. for 60 s and treated at 150 ˚C for 30 min in air. Then, the QD solutions (5 mg·mL^{-1}) in hexane were spun-cast at 2,000 rpm. for 20 s. Next, the commercially available Al:ZnO nanoparticle solution was spun-cast on the QD layers at 1,500 rpm. for 20 s and treated at 100 ˚C for 5 min in air. Finally, a 100 nm aluminum top electrode was thermally evaporated at a rate of 1.5–2 Å·s^{-1}; the active areas were encapsulated with a UV photocurable epoxy resin from Lighting Enterprises (ELC4908-30) and a cover glass.

3 Results and discussion

Blue-light-emitting CdZnS/ZnS QDs were prepared using a two-step hot injection method [15]. Green-, orange-, and red-light-emitting CdSe/CdS/ZnS QDs were synthesized through a one-step hot injection protocol with slight modifications [34]. See the Experimental section for further details.

Figure 1(a) shows the PL spectra of the synthesized core–shell QDs, which cover the entire visible spectrum. The emission spectra are centered at 466 (blue), 549 (green), 582 (orange), and 630 nm (red), respectively, and are very narrow in shape, especially that for the blue-light-emitting QDs (full width at half-maximum (FWHM) = 24 nm). The maximum emission wavelength and FWHM of the PL spectra and PL quantum yield values (Φ_f) are summarized in Table 1.

Figure 1(b) shows a high-resolution transmission electron microscopy (HR-TEM) image of the blue QDs; these QDs clearly show a very homogeneous size distribution with sizes below 10 nm. The size homogeneity of the blue QDs demonstrated in the HR-TEM image is corroborated by the narrowness of their PL spectrum, which shows a FWHM of only 24 nm, as noted above. Figure S1 (in the Electronic Supplementary Material (ESM)) shows HR-TEM images of the blue, green, orange, and red QDs at different magnifications. The results of energy-dispersive X-ray analysis confirm the different elemental compositions of the QDs. The HR-TEM images also reveal that the blue QDs are

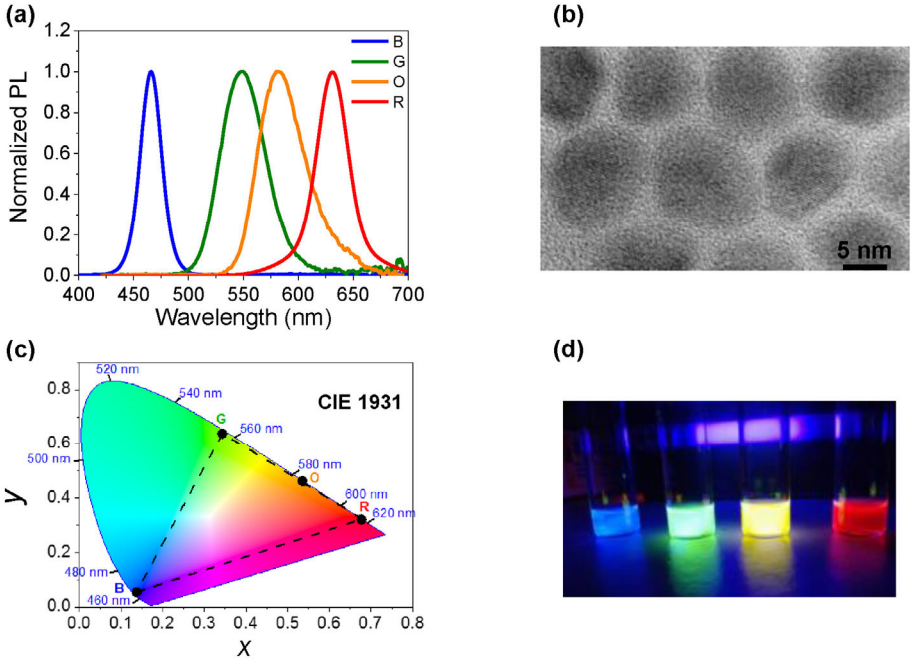

Figure 1 (a) PL spectra of visible-light-emitting QDs: blue (B), green (G), orange (O), and red (R). (b) HR-TEM image of the blue QDs at a magnification of 600,000 ×. (c) Chromaticity diagram (CIE 1931) showing the values corresponding to the blue, green, orange, and red QDs. Dashed triangle indicates the color gamut resulting from mixing the QDs. (d) Image of QD solutions diluted in hexane under UV light.

Table 1 Wavelength maxima, FWHMs, and Φ_f values of the QDs in hexane. The concentration was adjusted by fixing the absorbance at the excitation wavelength below 0.05 units. The Φ_f values were determined by comparison with a fluorescence standard: 9,10-diphenylanthracene (DPA) in ethanol for the blue QDs and coumarin (C-153) for the green, orange, and red QDs

Sample	λ_{max} (nm)	FWHM (nm)	Φ_f (λ_{exc})
Blue	466	24	0.55 (370 nm)[a]
Green	549	45	0.51 (405 nm)[b]
Orange	582	52	0.36 (405 nm)[b]
Red	630	37	0.29 (405 nm)[b]

a) DPA as fluorescence standard in ethanol (Φ_f = 0.91) [15],
b) C-153 as fluorescence standard in ethanol (Φ_f = 0.54) [35].

more spherical than the green, orange, and red ones; the difference is ascribed to the different synthesis methodology employed.

The PL spectra of the synthesized QDs were transformed into the corresponding chromaticity indexes and plotted in the CIE 1931 color space chromaticity diagram. As shown in Fig. 1(c), the black dots, which represent the chromaticity indices corresponding to the blue, green, orange, and red QDs, are located near the curved edge, indicating the pure color of the emitted light.

After the visible-light-emitting QDs were synthesized and characterized, a series of multicolored LEDs using the QDs as the light-emitting material were prepared and exhaustively analyzed. We used the standard device configuration by spin-casting the suitable materials. Figure 2(a) shows a rough approximation of the energy level alignment of the materials employed, and Fig. 2(b) presents a photograph of the multicolored LEDs at 7 V connected in parallel. To assemble the devices, a PEDOT:PSS layer was deposited onto a prepatterned ITO substrate (20 × 20 mm^2) as the HIL. Then, a thin layer of PVK was deposited as the HTM, followed by successive spin-casting of the QDs in hexane (5 mg·mL^{-1}). Al:ZnO nanoparticles were used as an ETM and hole-blocking layer. Finally, an aluminum electrode was thermally evaporated on top of the Al:ZnO layer. The active area of the devices was encapsulated with an epoxy resin in a glovebox to avoid premature degradation.

The single-color LEDs were individually characterized to study their performance. Figure 3 shows the

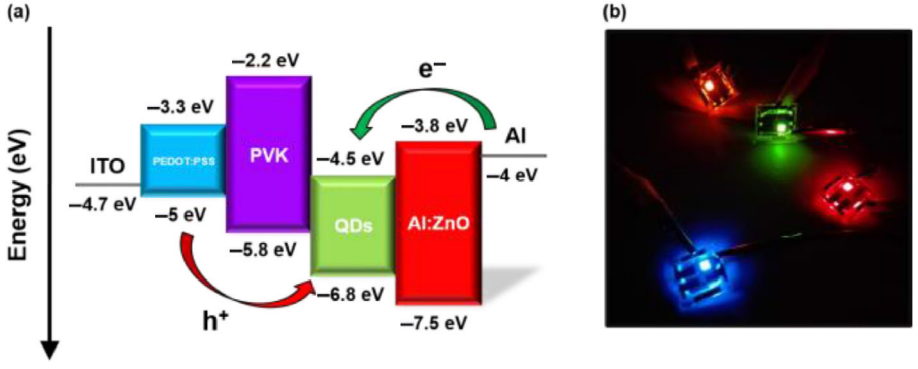

Figure 2 (a) Energy diagram of the materials employed for preparation of the QD-LEDs. The band energy values of the QDs in the diagram correspond to those of the green-light-emitting nanocrystals (≈ 2.3 eV). (b) Bright multicolored QD-LEDs driven at 7 V.

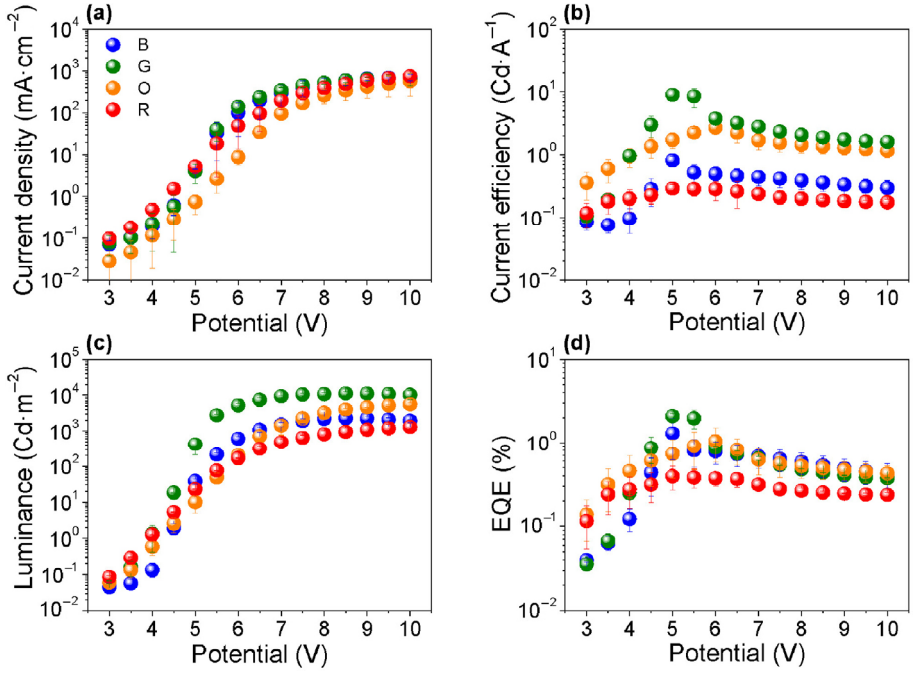

Figure 3 QD-LED performance: (a) current density (*J*–*V*) curves, (b) current efficiency, (c) luminance, and (d) EQE.

electro-optical response of the blue-, green-, orange-, and red-light-emitting devices. The data were obtained by analyzing eight different devices each for the blue, green, orange, and red LEDs, and thus present a reliable picture of their performance and the reproducibility of the preparation. Note that the performance values shown in Fig. 3 and Table 2 correspond to those obtained upon two consecutive voltage scans, as the first scans yield values slightly lower than those obtained in the second.

The *J*–*V* curves plotted in Fig. 3(a) show very similar behavior regardless of the QDs employed. The slight variations observed in the current densities could be ascribed to negligible differences in the concentrations of the QD solutions, which yield small deviations in the layer thicknesses. Other parameters such as the quality of the QDs or experimental errors arising during layer deposition could also contribute to the observed variations, although as a general trend, the error bars overlap at the various potential values displayed. Figure 3(b) reveals significant variations of the current efficiency depending on the QDs employed. The maximum value, 9.0 $Cd \cdot A^{-1}$, was observed for the green QDs. The data plotted in Fig. 3(c) show that the maximum luminance values range from 1,295 $Cd \cdot m^{-2}$ for the red QDs to 11,211 $Cd \cdot m^{-2}$ for the green ones.

Table 2 λ_{max} of the EL spectra at 5 V and maximum current efficiency, luminance, and EQE at the indicated potentials for the single-color QD-LEDs. All the performance values correspond to those obtained from two consecutive voltage scans (from 3 to 10 V)

QD-LED	λ_{max} (nm)	Current eff. ($Cd \cdot A^{-1}$)	Luminance ($Cd \cdot m^{-2}$)	EQE (%)
Blue	471	0.81 @ 5 V	2,284 @ 8.5 V	1.30 @ 5 V
Green	560	9.00 @ 5 V	11,211 @ 8.5 V	2.10 @ 5 V
Orange	591	2.70 @ 5 V	5,605 @ 10 V	1.04 @ 6 V
Red	622	0.29 @ 5 V	1,295 @ 10 V	0.39 @ 5 V

Similarly, the maximum EQE values range from 0.39% for the red QDs to 2.10% for the green QDs. Note that all the devices show turn-on voltages of around 3 V regardless of the type of QDs employed. Table 2 summarizes the performance results, showing the maximum values at the given potentials.

In conclusion, the overall performance of an LED is determined by the balance between the PL quantum yield of the QDs, which in this case is more favorable for larger-bandgap nanocrystals (Table 1), and the energy level alignment of the charge-selective contact, which is more favorable for small-bandgap QDs. After our exhaustive analysis, we conclude that green QDs exhibit the highest performance.

After the QD-LEDs with various colors were individually characterized, QD-WLEDs were prepared by mixing red, green, and blue or orange, green, and blue QDs. Figure 4 shows the performance of the QD-WLEDs based on the RGB and OGB approaches. In both cases, the solutions were 1:1:1 (volume) mixtures of the individual QD solutions at a fixed concentration (5 $mg \cdot mL^{-1}$).

As shown in Fig. 4(a), the *J*–*V* curves of the RGB and OGB devices show similar characteristics, with slight variations in the region between 4 and 6 V. In any case, the behavior and magnitude of the current values are in the same range as those obtained for the single-color devices (see Fig. 3(a)). Figure 4(b) shows the current efficiency, the maximum values of which are 1.74 $Cd \cdot A^{-1}$ for the OGB device and 0.45 $Cd \cdot A^{-1}$ for the RGB device. The data plotted in Fig. 4(c) show the luminance, the maximum values of which are 10,718 and 3,651 $Cd \cdot m^{-2}$ for the OGB and RGB devices, respectively. Figure 4(d) shows the EQE; the maximum EQEs are 0.65% and 0.18% for the OGB and RGB devices, respectively. Note that all the devices show turn-on voltages of around 3 V and thus behave similarly to the single-color devices previously analyzed.

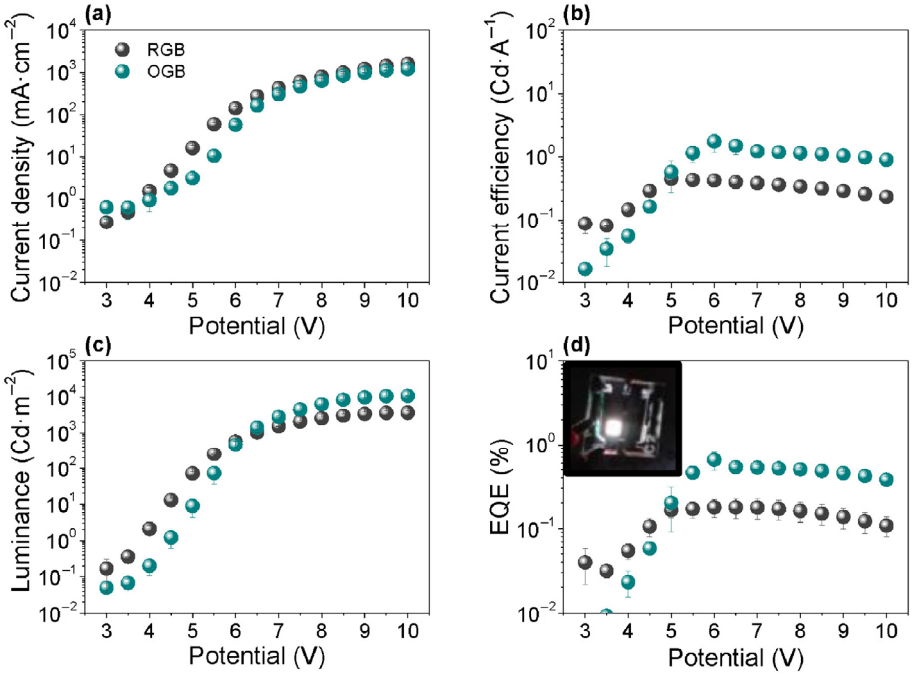

Figure 4 QD-WLED performance: (a) current density curves (*J*–*V*), (b) current efficiency, (c) luminance, and (d) EQE. Inset shows a working device (RGB) at 7 V.

The lighting industry provides two main metrics to communicate the color properties of a white light source, the correlated color temperature (CCT) and color rendering index (CRI) [36, 37]. The color temperature (CT) of a light source is the temperature in kelvins at which the color of a heated black body radiator matches the color of the light source; on heating, a black body initially becomes deep red at low temperatures and eventually becomes blue-white at very high temperatures. The CT characteristics of an incandescent bulb can be approximated by those of a black body because the tungsten filament inside the bulb radiates light at high temperature. However, fluorescent sources or WLEDs exploit other physical principles to generate white light and thus require a more appropriate definition of the color temperature, the CCT. The CCT is defined as the temperature of a black body radiator whose chromaticity is closest to that of the light emitted by the source. Lights with a CCT below 3,200 K show yellow-orange tonalities and are designed as warm white lights. Cool white lights are observed as blue-white, and their CCTs are above 4,000 K. White lights between approximately 3,200 and 4,000 K are considered neutral. Although the CCT is generally a good indicator of the light's appearance, it does not provide information about the spectral distribution of the illumination. Note that the CCT of the QD-WLEDs can be tuned by varying the ratios of the different QDs. To provide a more accurate metric of the spectral power distribution of a white light source, the CRI was defined. The CRI is the ability of a white light source to reproduce colors faithfully in comparison to a reference light of similar color temperature. Consequently, the color of an object illuminated by two white lights showing the same CCT but different CRIs can be perceived very differently because of the different spectral power distributions. In general, light sources with CRI values above 80% are considered to provide good color rendering.

An important issue to analyze when studying WLEDs is the stability of the white light properties. We studied the evolution of the chromaticity indices (the CCT and CRI) with the applied potential during consecutive measurements. Figures 5(a) and 5(d) show the EL spectra of the QD-WLEDs prepared using the RGB and OGB approaches, respectively. Although the shapes of the spectra differ significantly, both strategies yield light-emitting devices that cover the entire visible spectrum; the RGB devices show three

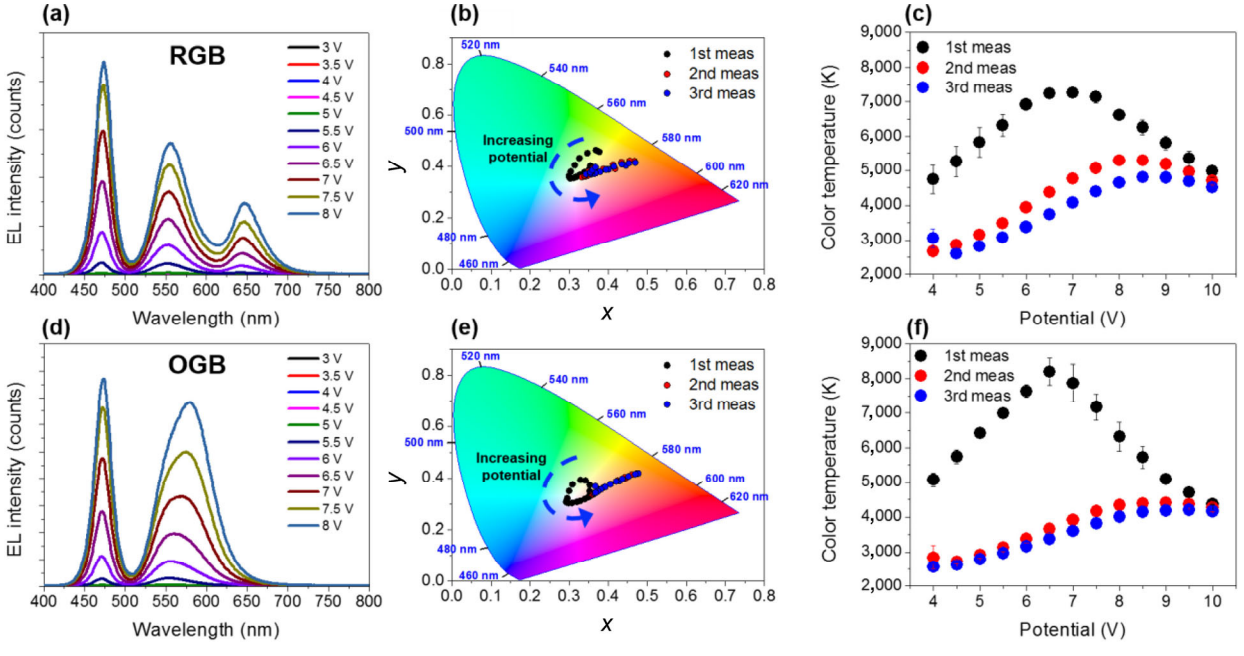

Figure 5 Performance of the QD-WLEDs based on the RGB and OGB approaches: (a), (d) EL spectra at different potentials; (b), (e) evolution of the chromaticity index (CIE 1931) with increasing potential after consecutive measurements; (c), (f) evolution of the CCT with the potential after consecutive measurements.

well-differentiated emission maxima at 471, 552, and 642 nm, whereas the OGB devices show a maximum at 471 nm and a broad combined signal between 500 and 700 nm that arises from the overlapping green and orange QD emission.

Figures 5(b) and 5(e) show the evolution of the chromaticity index (CIE 1931) with increasing potential during consecutive measurements. The chromaticity indices are clearly located near the center of the color diagram, thus revealing the whiteness of the light emitted by both the RGB and OGB devices. In addition, another similarity between the two approaches is observed; in the first measurement, the chromaticity index evolves from the yellowish region at low potentials to the reddish region at high potentials, passing through the bluish-white region at intermediate potentials. However, in subsequent measurements, the chromaticity index is less sensitive to the potential, although a clear variation at low potentials from the white region to the reddish region is observed. Note that after the first measurement, although the color of the emitted light varies with the applied potential, the same behavior is maintained during consecutive measurements, thus demonstrating partial stabilization of device operation after the first cycle. Nevertheless, a similar variation of the chromaticity index has been identified for longer operation periods at constant voltage. Figure S2 (in the ESM) shows a shift in the color coordinates from the bluish region to the reddish, thus revealing continuous evolution of the devices under long-term working conditions. In addition, Figs. 5(c) and 5(f) show the evolution of the CCT at different applied potentials in consecutive measurement cycles. In this case, the first measurements show maximum CCT values of 7,265 and 8,200 K for the RGB and OGB devices, respectively. However, after the first measurement, the CCT is significantly lower, and it is stabilized at around 5,291 K for the RGB devices and 4,409 K for the OGB devices. Figure 6 shows the CRIs of the OGB and RGB devices measured at different potentials during three consecutive measurements. For the OGB samples (Fig. 6(a)), a maximum CRI of 60% was obtained; however, the RGB samples (Fig. 6(b)) yield a significantly enhanced value exceeding 80% over a wide range of potentials. High CRI values are especially important for certain applications, such as photography and cinematography, that require reliable reproduction of colors.

In summary, our RGB devices show better light quality than the OGB devices, although their EQE is lower. A straightforward strategy to improve the CRI of our QD-WLEDs should be based on synthesizing green-emitting QDs with chromaticity indices in the upper region of the CIE diagram, thus increasing the gamut of the emitted white light and consequently the CRI. However, increasing the color gamut excessively may lead to oversaturated colors that could cause an unnatural perception of colors by the human eye. The main approach to improving the EQE involves modification of the experimental conditions of QD synthesis to obtain higher-quality nanocrystals with enhanced radiative charge recombination, to the detriment of nonradiative pathways.

To elucidate the origins of the color variations observed in our QD-WLEDs, we designed a series of experiments. First, the transient PL decay of the QD films, including those of the RGB and OGB QD mixtures, were measured using a nanosecond-pulsed Nd:YAG laser as an excitation source (λ_{exc} = 410 nm). Table 3 shows the decay time constants of the QD samples extracted from the corresponding decays, as shown in Fig. S3 (in the ESM).

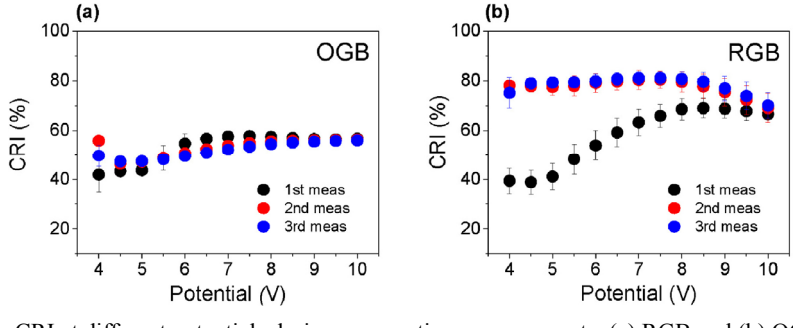

Figure 6 Evolution of the CRI at different potentials during consecutive measurements: (a) RGB and (b) OGB devices.

Table 3 Time constants extracted from the PL decays (λ_{exc} = 410 nm) at different λ_{det} depending on the QD emission region

Sample	λ_{det} (nm)	τ_1 (ns)	τ_2 (ns)
Blue	470	11.1	71.8
Green	550	28.5	n.d.*
Orange	580	10.3	n.d.*
Red	630	8.6	n.d.*
RGB	470	7.5	43.7
RGB	550	13.7	n.d.*
RGB	630	12.5	n.d.*
OGB	470	8.2	51.8
OGB	550	17.4	n.d.*
OGB	580	17.1	n.d.*

*n.d. not detected: The data are fitted to a single exponential function.

The measured PL decay time constants of the films are on the order of a few nanoseconds; thus, they are in agreement with those found in Ref. [25]. In particular, the decays of the blue QDs were fitted by a double exponential function, and therefore, two time constants were obtained. In contrast, the decays of the green, orange, and red films were fitted by a single exponential function. These results clearly show that the time constants of the blue and green components of the RGB and OGB films are faster than those of the blue and green single-color films. In contrast, the red and orange components of the RGB and OGB films are slower than those obtained from the corresponding single-color films. These observations indicate that there is significant interaction among QDs with different bandgaps, which is reasonable, because wider-bandgap QDs can transfer energy or even charges themselves to QDs with narrower bandgaps. These nonradiative energy or charge transfer phenomena could clearly contribute to the lower performance of the RGB and OGB QD-WLEDs compared to the single-color devices; however, because the fluorescent resonance energy transfer mechanisms are independent of the local donor concentration, this could not explain the evolution of the white light characteristics with increasing applied potential. To further explore this phenomenon, we show in Fig. S4 (in the ESM) the EL of the single-color QD light-emitting devices at different applied potentials, which demonstrates that the EL intensity depends not only on the potential but also on the nature of the QDs employed. The green and blue QDs show the highest EL values at a given potential, whereas the red and orange QDs show significantly lower values. As shown in Fig. S4 (in the ESM), the EL signal of the green- and blue-emitting devices starts to saturate at approximately 8 V; however, the EL intensity of the orange and red devices continues to increase even at the highest potentials. These results are consistent with the fact that at low potentials, the CIE values shift to the green region of the chromaticity diagram, evolving gradually to the blue region as the voltage increases and finally shifting to the reddish or orange region at higher voltages. We also studied the evolution of the EQE of the single-color QD-LEDs at constant voltage (5 V) over time. Figure S5 (in the ESM) clearly demonstrates that the EQE evolution depends on the type of QD; the blue-emitting devices show the maximum EQE at the very beginning of the experiment, and the EQE decreases gradually over time. In contrast, the green-, orange-, and red-emitting LEDs show an initial increase in the EQE within approximately the first 2.5 h, and then the EQE starts decreasing gradually. Note that the EQE deactivation rate of the red- and orange-emitting LEDs at constant voltage (5 V) is slower than that observed for the blue and green devices, which accounts for the observed evolution of the chromaticity indices of the RGB and OGB devices shown in Fig. S2 (in the ESM). Therefore, these results point to the variation in the EL behavior depending on the applied potential or the time evolution depending on the type of QD as the main origin of the observed evolution of the white light characteristics of the RGB and OGB devices.

In addition to the efficiency, color characteristics, and related experimental variables, there are other parameters that should be carefully analyzed for the development of light-emitting devices or displays. Specifically, the response time of the devices is a crucial characteristic to consider [29]. In this work, we measured the turn-on and turn-off response times of our single-color QD-LEDs and QD-WLEDs. To measure the response times, we applied a square wave potential function of constant amplitude and frequency (7 V and 50 Hz, respectively), and we

measured the emitted light using a fast-response photodiode connected to an oscilloscope. Figure 7 shows the typical response of our LEDs.

The response times extracted from the exponential fittings are shown in Table S1 (in the ESM). The turn-on time constants are on the order of 100 μs, whereas the turn-off values are approximately 180 μs. Further, a remarkable overshoot feature is observed in the turn-on region of the response function (Fig. 7), which is detected in all the devices measured in this work. We ascribe this overshoot to the unbalanced charge injection on both sides of the QD layer. The energy diagram in Fig. 2(a) clearly shows that the energy barrier for the hole injection process is significantly higher than that for electron injection. Therefore, we suggest that when an external potential is applied, electrons are swiftly injected into and accumulated in the QDs, and radiative recombination occurs only after the hole injection energy barrier is exceeded. In the initial stage, the injected holes recombine very efficiently with the excess accumulated electrons, yielding enhanced light output; however, after a few milliseconds, the accumulated electrons disappear, and the optical signal reaches equilibrium. The overshoot decay was fitted to a mono-exponential function, which yielded a characteristic time of 1.1 ms. Although this is outside the scope of this work, the overshoot features should be removed by decreasing the hole injection barriers, which in turn should improve the efficiency of our devices. An excess of one type of carrier in the QD region results in charge accumulation in the QD layer, which increases the probability of nonradiative three-body Auger relaxation, thus limiting the efficiency of radiative recombination [38].

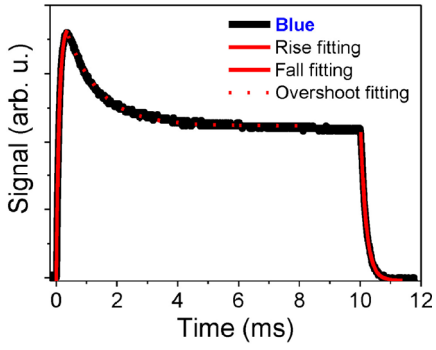

Figure 7 Response time function of our QD-LED with emission in the blue region. Solid red lines show the exponential fittings used to calculate the turn-on and turn-off response times, and dotted red line shows the overshoot fitting.

Finally, we studied the stability of the QD-LEDs during long operational periods; in particular, we measured the optical signal emitted from our devices while an external potential (5 V) was applied continuously for 20 h. Figure 8(a) shows the evolution of the EL intensity (red line) and the current density (black line) of a green-light-emitting device with the aging time at a constant potential. The emitted light intensity clearly decreases over the aging period, reaching 50% of the initial intensity after 5.4 h of continuous operation. After 20 h, the remaining signal is almost 30% of the initial signal, suggesting the relative stability of our devices. Note that the decrease in the EL is accompanied by a significant decrease in the overall current density flowing through the device. In fact, an increase in the normalized EQE is observed during the first 2.5 h, followed by a gradual decrease at longer intervals (Fig. S5 (in the ESM)).

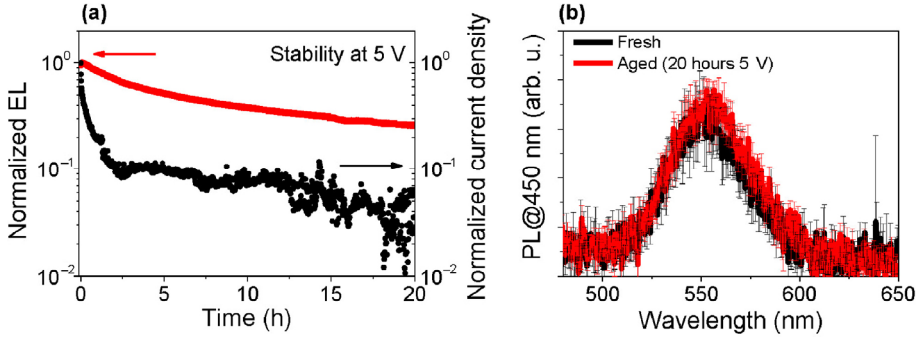

Figure 8 (a) Normalized EL intensity (red line) and current density (black line) of a green-light-emitting QD-LED as a function of the aging time at 5 V. (b) Absolute PL spectra of the green QDs inserted in the active area of a complete device (λ_{exc} = 450 nm) before and after aging at 5 V for 20 h. Vertical bars indicate the measurement error at each wavelength.

To further explore the origins of the relative but limited stability of our devices, we measured the PL of the active area of the green-light-emitting working device before and after aging at 5 V for 20 h. Figure 8(b) shows the absolute PL signals of the green-light-emitting QDs before and after aging of the device; the PL signal of the QDs clearly remains unchanged after the aging process, which demonstrates that the QDs are completely stable under long-term operation. Therefore, the decrease in the EL and current density cannot be ascribed to degradation of the light-active material, i.e., QDs. Some precedents in the literature suggest that the acidic nature of PEDOT:PSS may damage the interface with ITO [39–41]. In fact, our results point clearly to that hypothesis, because degradation of the PEDOT:PSS/ITO interface would lead to a significant decrease in the current density and EL intensity of the system (Fig. 8(a)). Future works will focus on chemical treatment of the PEDOT:PSS layer to decrease its acidity or even on its replacement with an alternative HIL. The degradation of the HIL has important implications for the device performance, not only because the intensity of the emitted light decreases, but also because it might induce significant variation of the white light color of mixed-QD WLEDs. If the PEDOT:PSS/ITO interface degrades, charge injection at a given potential becomes less likely, and therefore, the current density is lowered, as demonstrated in Fig. 8(a). For the single-color devices, this affects only the intensity of the emitted light; however, different behavior is observed for the QD-WLEDs. In the latter case, when charge injection is gradually hampered, the charge carriers are injected more selectively to the QDs with narrower bandgaps because the energy barriers are lower. This behavior promotes a gradual variation of the chromaticity indices toward the reddish region, as shown in Fig. S2 (in the ESM), because the red component of the EL spectrum becomes gradually more intense compared to the blue and green components. Therefore, maintaining a constant charge injection efficiency for a long period not only ensures constant EL intensity but also good stability of the white light characteristics.

4 Conclusions

In summary, we prepared and characterized bright visible-light-emitting devices covering the entire visible spectrum, including white LEDs prepared through two different approaches, RGB and OGB. Very importantly, we provide new insights on the performance of the QD-WLEDs, suggesting two feasible mechanisms that account for the observed variations of the white light characteristics. First, the energy and/or charge transfer mechanisms from QDs with a wider bandgap toward those with a narrower bandgap are to some extent responsible for the limited efficiency of the RGB and OGB devices compared to the single-color QD-LEDs. Second, we demonstrated that the different EL intensities of the blue, green, orange, and red QD-LEDs at the scanned potentials account for the evolution of the chromaticity indices of the RGB and OGB devices when the potential is increased. Additionally, we demonstrated that the QDs are totally stable over long operation periods (> 20 h) at constant voltage; however, our results suggest degradation of the PEDOT:PSS/ITO interface, which causes limited charge injection into the wider-bandgap QDs, thus contributing to the variation of the white light characteristics from the white region of the diagram to the reddish. These phenomena have scarcely been explored to date, and we suggest that replacing the PEDOT:PSS with an alternative HIL would lead not only to more stable devices, but also to QD-WLEDs with more reliable white light characteristics. Finally, we contribute valuable information about the characterization of the response time and life time of the QD-LEDs. Note that all these studies are crucial to the development of the next generation of ultrathin bright electroluminescent displays with the extremely wide palette of colors that inorganic QDs may afford.

Acknowledgements

The work was supported by MINECO of Spain (No. MAT2016-76892-C3-1-R) and by Generalitat Valenciana (No. PROMETEOII/2014/020). B. C. H. is grateful to the support of the National Council of Technological and Scientific Development (CNPq), Brazil, through the Science without Borders program.

Electronic Supplementary Material: Supplementary

material (characterization equipment, HR-TEM images, evolution of the chromaticity indexes, transient PL decay of the blue QDs film, EL at different applied potentials, evolution of the normalized EQE, response time of the turn-on and turn-off processes) is available in the online version of this article at https://doi.org/10.1007/s12274-017-1773-2.

References

[1] Ekimov, A. I.; Onushchenko, A. A. Quantum size effect in three-dimensional microscopic semiconductor crystals. *J. Exp. Theoret. Phys. Lett.* **1981**, *34*, 345.

[2] Derfus, A. M.; Chan, W. C. W.; Bhatia, S. N. Probing the cytotoxicity of semiconductor quantum dots. *Nano Lett.* **2004**, *4*, 11–18.

[3] Jamieson, T.; Bakhshi, R.; Petrova, D.; Pocock, R.; Imani, M.; Seifalian, A. M. Biological applications of quantum dots. *Biomaterials* **2007**, *28*, 4717–4732.

[4] Ko, D. K.; Maurano, A.; Suh, S. K.; Kim, D.; Hwang, G. W.; Grossman, J. C.; Bulović, V.; Bawendi, M. G. Photovoltaic performance of PBS quantum dots treated with metal salts. *ACS Nano* **2016**, *10*, 3382–3388.

[5] Li, X. M.; Wu, Y.; Zhang, S. L.; Cai, B.; Gu, Y.; Song, J. Z.; Zeng, H. B. Quantum dots: $CsPbX_3$ quantum dots for lighting and displays: Room-temperature synthesis, photoluminescence superiorities, underlying origins and white light-emitting diodes. *Adv. Funct. Mater.* **2016**, *26*, 2584.

[6] Liu, M. X.; Voznyy, O.; Sabatini, R.; de Arquer, F. P. G.; Munir, R.; Balawi, A. H.; Lan, X. Z.; Fan, F. J.; Walters, G.; Kirmani, A. R. et al. Hybrid organic–inorganic inks flatten the energy landscape in colloidal quantum dot solids. *Nat. Mater.* **2017**, *16*, 258–263.

[7] Liu, M. X.; de Arquer, F. P. G.; Li, Y. Y.; Lan, X. Z.; Kim, G. H.; Voznyy, O.; Jagadamma, L. K.; Abbas, A. S.; Hoogland, S.; Lu, Z. H. et al. Double-sided junctions enable high-performance colloidal-quantum-dot photovoltaics. *Adv. Mater.* **2016**, *28*, 4142–4148.

[8] Kim, G. H.; de Arquer, F. P. G.; Yoon, Y. J.; Lan, X. Z.; Liu, M. X.; Voznyy, O.; Yang, Z. Y.; Fan, F. J.; Ip, A. H.; Kanjanaboos, P. et al. High-efficiency colloidal quantum dot photovoltaics via robust self-assembled monolayers. *Nano Lett.* **2015**, *15*, 7691–7696.

[9] Rekemeyer, P. H.; Chang, S.; Chuang, C. H. M.; Hwang, G. W.; Bawendi, M. G.; Gradečak, S. Enhanced photocurrent in pbs quantum dot photovoltaics via ZnO nanowires and band alignment engineering. *Advanced Energy Materials* **2016**, *6*, 1600848.

[10] Sargent, E.; McDonald, S. A.; Zhang, S. G.; Levina, L.; Konstantatos, G.; Cyr, P. Three-dimensional bicontinuous heterostructures, method of making, and their application in quantum dot-polymer nanocomposite photodetectors and photovoltaics. U. S. Patents 20130244366, September 19, 2013.

[11] Lhuillier, E.; Scarafagio, M.; Hease, P.; Nadal, B.; Aubin, H.; Xu, X. Z.; Lequeux, N.; Patriarche, G.; Ithurria, S.; Dubertret, B. Infrared photodetection based on colloidal quantum-dot films with high mobility and optical absorption up to thz. *Nano Lett.* **2016**, *16*, 1282–1286.

[12] Hwang, D. K.; Lee, Y. T.; Lee, H. S.; Lee, Y. J.; Shokouh, S. H.; Kyhm, J. h.; Lee, J.; Kim, H. H.; Yoo, T. H.; Nam, S. H. et al. Ultrasensitive pbs quantum-dot-sensitized InGaZnO hybrid photoinverter for near-infrared detection and imaging with high photogain. *NPG Asia Mater.* **2016**, *8*, e233.

[13] Gao, J. B.; Nguyen, S. C.; Bronstein, N. D.; Alivisatos, A. P. Solution-processed, high-speed, and high-quantum-efficiency quantum dot infrared photodetectors. *ACS Photonics* **2016**, *3*, 1217–1222.

[14] Mashford, B. S.; Stevenson, M.; Popovic, Z.; Hamilton, C.; Zhou, Z. Q.; Breen, C.; Steckel, J.; Bulovic, V.; Bawendi, M.; Coe-Sullivan, S. et al. High-efficiency quantum-dot light-emitting devices with enhanced charge injection. *Nat. Photonics* **2013**, *7*, 407–412.

[15] Lee, K. H.; Lee, J. H.; Song, W. S.; Ko, H.; Lee, C.; Lee, J. H.; Yang, H. Highly efficient, color-pure, color-stable blue quantum dot light-emitting devices. *ACS Nano* **2013**, *7*, 7295–7302.

[16] Lee, K. H.; Lee, J. H.; Kang, H. D.; Park, B.; Kwon, Y.; Ko, H.; Lee, C.; Lee, J.; Yang, H. Over 40 cd/a efficient green quantum dot electroluminescent device comprising uniquely large-sized quantum dots. *ACS Nano* **2014**, *8*, 4893–4901.

[17] Zhang, H.; Wang, S. T.; Sun, X. W.; Chen, S. M. Solution-processed vanadium oxide as an efficient hole injection layer for quantum-dot light-emitting diodes. *J. Mater. Chem. C* **2017**, *5*, 817–823.

[18] Dai, X. L.; Zhang, Z. X.; Jin, Y. Z.; Niu, Y.; Cao, H. J.; Liang, X. Y.; Chen, L. W.; Wang, J. P.; Peng, X. G. Solution-processed, high-performance light-emitting diodes based on quantum dots. *Nature* **2014**, *515*, 96–99.

[19] Sanchez, R. S.; Binetti, E.; Torre, J. A.; Garcia-Belmonte, G.; Striccoli, M.; Mora-Sero, I. All solution processed low turn-on voltage near infrared leds based on core–shell PbS-CdS quantum dots with inverted device structure. *Nanoscale* **2014**, *6*, 8551–8555.

[20] Anikeeva, P. O.; Halpert, J. E.; Bawendi, M. G.; Bulovic, V. Quantum dot light-emitting devices with electroluminescence tunable over the entire visible spectrum. *Nano Lett.* **2009**, *9*, 2532–2536.

[21] Moreels, I.; Justo, Y.; De Geyter, B.; Haustraete, K.; Martins, J. C.; Hens, Z. Size-tunable, bright, and stable PbS quantum dots: A surface chemistry study. *ACS Nano* **2011**, *5*, 2004–2012.

[22] Steckel, J. S.; Ho, J.; Hamilton, C.; Xi, J. Q.; Breen, C.; Liu, W. H.; Allen, P.; Coe-Sullivan, S. Quantum dots: The ultimate down-conversion material for LCD displays. *J. Soc. Inf. Display* **2015**, *23*, 294–305.

[23] Shirasaki, Y.; Supran, G. J.; Bawendi, M. G.; Bulović, V. Emergence of colloidal quantum-dot light-emitting technologies. *Nat. Photonics* **2013**, *7*, 13–23.

[24] Yang, Y. X.; Zheng, Y.; Cao, W. R.; Titov, A.; Hyvonen, J.; Manders, J. R.; Xue, J. G.; Holloway, P. H.; Qian, L. High-efficiency light-emitting devices based on quantum dots with tailored nanostructures. *Nat. Photonics* **2015**, *9*, 259–266.

[25] Lee, K. H.; Han, C. Y.; Kang, H. D.; Ko, H.; Lee, C.; Lee, J.; Myoung, N.; Yim, S. Y.; Yang, H. Highly efficient, color-reproducible full-color electroluminescent devices based on red/green/blue quantum dot-mixed multilayer. *ACS Nano* **2015**, *9*, 10941–10949.

[26] Han, J.; Bong, J.; Lim, T.; Lee, K. H.; Yang, H.; Ju, S. Water repellent spray-type encapsulation of quantum dot light-emitting diodes using super-hydrophobic self-assembled nanoparticles. *Appl. Surf. Sci.* **2015**, *353*, 338–341.

[27] Qian, L.; Zheng, Y.; Xue, J. G.; Holloway, P. H. Stable and efficient quantum-dot light-emitting diodes based on solution-processed multilayer structures. *Nat. Photonics* **2011**, *5*, 543–548.

[28] Bae, W. K.; Park, Y. S.; Lim, J.; Lee, D.; Padilha, L. A.; McDaniel, H.; Robel, I.; Lee, C.; Pietryga, J. M.; Klimov, V. I. Controlling the influence of auger recombination on the performance of quantum-dot light-emitting diodes. *Nat. Commun.* **2013**, *4*, 2661.

[29] Caruge, J. M.; Halpert, J. E.; Wood, V.; Bulović, V.; Bawendi, M. G. Colloidal quantum-dot light-emitting diodes with metal-oxide charge transport layers. *Nat. Photonics* **2008**, *2*, 247–250.

[30] Anikeeva, P. O.; Halpert, J. E.; Bawendi, M. G.; Bulović, V. Electroluminescence from a mixed red-green-blue colloidal quantum dot monolayer. *Nano Lett.* **2007**, *7*, 2196–2200.

[31] Kim, T. H.; Cho, K. S.; Lee, E. K.; Lee, S. J.; Chae, J.; Kim, J. W.; Kim, D. H.; Kwon, J. Y.; Amaratunga, G.; Lee, S. Y. et al. Full-colour quantum dot displays fabricated by transfer printing. *Nat. Photonics* **2011**, *5*, 176–182.

[32] Wood, V.; Panzer, M. J.; Chen, J. L.; Bradley, M. S.; Halpert, J. E.; Bawendi, M. G.; Bulović, V. Inkjet-printed quantum dot-polymer composites for full-color ac-driven displays. *Adv. Mater.* **2009**, *21*, 2151–2155.

[33] Kim, K.; Woo, J. Y.; Jeong, S.; Han, C. S. Photoenhancement of a quantum dot nanocomposite via uv annealing and its application to white leds. *Adv. Mater.* **2011**, *23*, 911–914.

[34] Bae, W. K.; Char, K.; Hur, H.; Lee, S. Single-step synthesis of quantum dots with chemical composition gradients. *Chem. Mater.* **2008**, *20*, 531–539.

[35] Rurack, K.; Spieles, M. Fluorescence quantum yields of a series of red and near-infrared dyes emitting at 600–1,000 nm. *Anal. Chem.* **2011**, *83*, 1232–1242.

[36] Bender, V. C.; Marchesan, T. B.; Alonso, J. M. Solid-state lighting: A concise review of the state of the art on led and oled modeling. *IEEE Ind. Electronics Mag.* **2015**, *9*, 6–16.

[37] Chen, H. T.; Hui, S. Y. Dynamic prediction of correlated color temperature and color rendering index of phosphor-coated white light-emitting diodes. *IEEE Trans. Ind. Electronics* **2014**, *61*, 784–797.

[38] Shimizu, K. T.; Woo, W. K.; Fisher, B. R.; Eisler, H. J.; Bawendi, M. G. Surface-enhanced emission from single semiconductor nanocrystals. *Phys. Rev. Lett.* **2002**, *89*, 117401.

[39] Murase, S.; Yang, Y. Solution processed moo3 interfacial layer for organic photovoltaics prepared by a facile synthesis method. *Adv. Mater.* **2012**, *24*, 2459–2462.

[40] Cho, A.; Kim, S.; Kim, S.; Cho, W.; Park, C.; Kim, F. S.; Kim, J. H. Influence of imidazole-based acidity control of PEDOT:PSS on its electrical properties and environmental stability. *J. Polym. Sci. B: Polym. Phys.* **2016**, *54*, 1530–1536.

[41] Jasieniak, J. J.; Seifter, J.; Jo, J.; Mates, T.; Heeger, A. J. A solution-processed MoO_x anode interlayer for use within organic photovoltaic devices. *Adv. Funct. Mater.* **2012**, *22*, 2594–2605.